13

High-Resolution Near-Field Optical Microscopy: A Sub-10 Nanometer Probe for Surface Electromagnetic Field and Local Dielectric Trait

Jen-You Chu[1] and Juen-Kai Wang[2,3]
[1]*Material and Chemical Research Laboratories*
Industrial Technology Research Institute, Hsinchu
[2]*Center for Condensed Matter Sciences, National Taiwan University, Taipei*
[3]*Institute of Atomic and Molecular Sciences, Academia Sinica, Taipei*
Taiwan

1. Introduction

The first optical microscope was made by Zacharias Janssen in the late sixteenth century. Robert Hooke used his own microscope to observe bio-samples and draw these structures on the micrographia in the seventeenth century. August Köhler, in 1893, developed an illumination technique, allowing for even sample lighting and setting the corner stone for modern light microscopy. In 1930s, Zeiss laboratory invented the upright microscope that is a prototype of modern optical microscopy. Such earlier effort to extend human vision in examining tiny objects is however limited by wave diffraction, as pointed out by Helmholtz and Abbe [1]. Namely, in visible wavelength range, optical resolution is about 250 nm. Such resolution limit certainly does not satisfy the need for current development and progress of nanotechnology, in which objects within 100 nm portray unique properties and functions that are not predictable by direct extrapolation from their macro-counterparts. It is thus crucial to extend the optical resolution below the Abbe's limit if we want to further the role of optical microscopy in future technology advance.

Although both electron microscopy and scanning probe microscopy easily meet the resolution requirement for nanotechnology, optical microscopy provides two unique characteristics that are not possible by them. First, optical microscopy is a noninvasive characterization method and can therefore examine objects in ambient environment or through transparent condensed media. Second, the energy resolving power of an optical probe surpasses the other two microscopic techniques, greatly enhancing its species identification ability in conjunction with various spectroscopic probes. These two distinctive capabilities are promised to more clearly unravel the novel relationship between the size/shape of a nano-object and its property which is essential to the advancement of nanotechnology, if the spatial resolution of optical microscopy can reach sub-10 nanometer scale.

A dramatic improvement of optical resolution has become possible by the invention of aperture-type scanning near-field optical microscopy (SNOM) [2-5]. Viewing through a tiny pinhole, firstly proposed by Synge [6] in 1928, spurs a series of attempts to realize such

concept. In 1984, two groups have simultaneously demonstrated it in the visible wavelength range [7-8]. Light through a sub-wavelength diameter aperture, which is evanescent in character, illuminates a sample within its near-field range. The optical response thus recorded while the sample is scanned laterally constructs a near-field optical image – scanning near-field optical microscope (SNOM). Its resolution depends on the diameter of aperture. Although breaking the Abbe's resolution limit, this new type of optical microscope holds three restrictions. The first one is that the resolution cannot be better than 50 nm, caused by the finite penetration into the optical field-confinement metal structure that defines the aperture. The second one is the trade-off between spatial resolution and collected signal intensity – the smaller the aperture is, the smaller the optical signal is collected [9]. The third one is that the throughput of the aperture is highly wavelength dependent, thus distorting the recorded optical spectrum. The aforementioned restrictions thus restrain the practice of aperture-type SNOM from the applications in nanophotonics and nanotechnology in general.

In contrast to the aperture-type SNOM, Wickramasinghe and coworkers in 1994 demonstrated an apertureless SNOM with a 10-nm resolution on the basis of sensing the dipole-dipole coupling between a tip end and a sample [10]. Later, Keilmann's team furthermore extended this approach to extract both amplitude and phase of such electromagnetic coupling simultaneously, concocting a comprehensive scattering-type SNOM (*s*-SNOM) [11-15], as depicted in Fig. 1. The collimated optical radiation impinges onto the site where the apex of an atomic force microscopic tip (AFM probe) is in close proximity of sample surface (enclosed by green dotted ellipse). Right-handed image of the figure 1 shows a blow-up view of the induced localized field at the tip apex. The restrictions of aperture-type SNOM are unleashed in such new-generation SNOM. Firstly, the resolution of s-SNOM is only limited by the tip radius. Secondly, the enhanced local field at the tip apex, owing to plasmon resonance, intensifies the electromagnetic interaction at the tip-sample system and thus boosts up the resulted scattered radiation for detection.

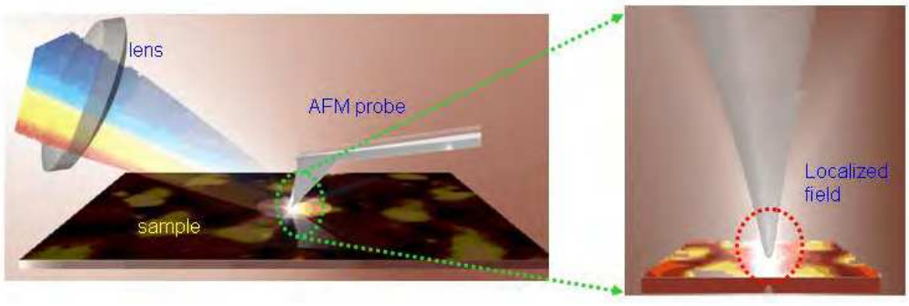

Fig. 1. Schematic view of scattering-type scanning near-field optical microscope.

In this chapter, we delineate the fundamental theory of *s*-SNOM (Section 2) and show its experimental setup (Section 3). Section 4 describes issues relevant to extracting near-field images. Its spatial resolution is demonstrated and discussed in Section 5. We show that *s*-SNOM is a powerful tool to unravel local optical properties in nanocomposite systems in Section 6. Furthermore in Section 7, we illustrate that it is possible to extract both amplitude and phase of surface plasmon polariton. The two cases above exemplify the great potential of *s*-SNOM to explore plasmonics and metamaterials, as well as nano-structured composite systems. Finally, Section 8 concludes this chapter.

2. Theory of *s*-SNOM

The field enhancement of a metallic tapered tip apex could be up to 1000-fold higher than the field of an incident optical wave that impinges onto it in an optimum condition for electromagnetic resonance [16]. As a consequence, the electromagnetic interaction between the tip and the incident field can be greatly altered owing to the presence of a near-by surface within the near-field enhancement zone, conferring an enhanced scattered radiation to the far field. Understanding the electromagnetic interaction taking place between the tip apex and the sample surface entails the detailed structure of the tip and solving the electromagnetic field in vicinity of the tip-surface composite system. Nonetheless, a simple model that can reveal the fundamental nature of such electromagnetic interaction would assist in understanding the limits of *s*-SNOM and in furthering its advancement and generalization. The first simplification is that only the response of the tip to the incident optical wave coming from the region around the tip apex is considered, whose dimension is much smaller than the wavelength of the incident wave, such that phase retardation is negligible over such region and thus a quasi-static treatment is justified [17-19]. Secondly, in spite that many multipole fields could be produced from the interaction between the incident wave and the tip apex of finite size and of complicated shape, only the dipole field from a sphere that approximates the tip apex is considered for it dominates the far-field radiation characteristics from the tip-surface system. Lastly, only a flat sample surface is considered for extracting the far-field scattered radiation, though a corrugated surface is expected to modify the outcome. The influence of the surface structure will be discussed later.

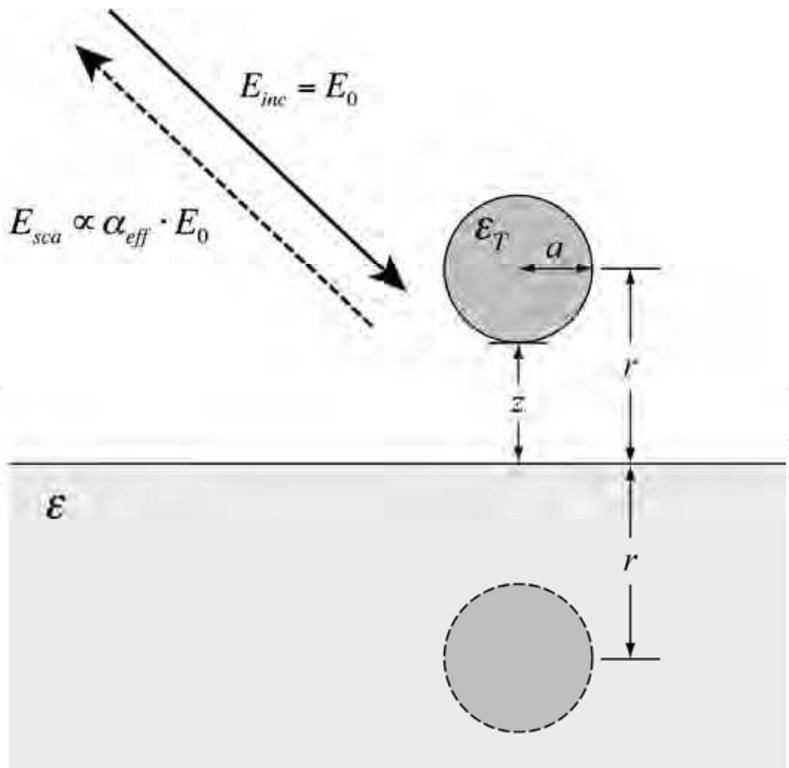

Fig. 2. Schematic of quasi-electrostatic dipole model illustrating the electromagnetic interaction happening in *s*-SNOM of side-illuminating geometry.

Figure 2 shows the geometric schematic of the interaction of a *p*-polarized incident electromagnetic wave with an electric field E_0 that impinges onto the surface with an incident angle θ_i. A sphere with a radius of *a* and a dielectric constant of ε_T that symbolizes the tip apex, residing at *r* above the surface of sample that has a dielectric constant of ε, in *s*-SNOM. The gap between the sphere and the surface is $z = r - a$. According to the Mie's theory of a sphere [20], the sphere illuminated by the incident light gives an induced point dipole with a dipole moment of *p* that is equal to $\alpha_T \cdot E_0$, where α_T is the polarizability of the sphere. As a consequence, such dipole at *r* above the surface induces an image dipole with a dipole moment of *p*′ that resides at *r* directly below the surface. The image dipole creates another dipole field that together with the incident field produces the dipole moment *p* [21]. An effective polarizability, α_{eff}, can then be derived by solving the resultant equation self-consistently. Accordingly, the scattered radiation of the incident wave from such tip-surface system can be considered is produced by the combination of the dipole and image dipole. Namely, α_{eff} of such combination is given by

$$\alpha_{eff} = \alpha_T \left(1 + \beta \cos 2\theta_i\right) F\left(r, \theta_i\right), \tag{1}$$

where

$$F\left(r, \theta_i\right) = \frac{1}{1 - \beta\left(\frac{\varepsilon_T - 1}{\varepsilon_T + 2}\right)\left(\frac{1 + \cos^2 \theta_i}{8}\right)\left(\frac{a}{a + z}\right)^3}, \tag{2}$$

$$\alpha_T = 4\pi a^3 \frac{\varepsilon_T - 1}{\varepsilon_T + 2}, \tag{3}$$

and

$$\beta = \left(\varepsilon - 1\right)/\left(\varepsilon + 1\right). \tag{4}$$

z is the separation between the tip apex and the sample surface and is equal to $r - a$ and, furthermore, and β is the ratio between the dipole moments of the dipole of the tip apex and the image dipole. The scattering light field, given by

$$E_{sca} \propto \alpha_{eff} \times E_0, \tag{5}$$

directly reflects α_{eff} – which conveys the dielectric property of the sample and the tip-sample separation – and the field E_0 that induces it. Consequently, *s*-SNOM can extract the distribution of the dielectric constant of the sample if the tip-sample separation is fixed, as well as the optical field at the surface if the sample is uniform. Figure 3 shows the calculated scattering intensity $|E_0|^2$ of a chromium sphere on the surfaces of Au, SiO2 and Si as a function of r/a based on Eq. (5). Two facts can be extracted from this figure. First, the scattering intensity is sensitive to the dielectric constant of the sample, engendering *s*-SNOM to be a local probe of the dielectric property. Second, the scattering intensity bears a near-field nature – it decreases almost exponentially to a plateau as $r/a \leq 1.5$. This feature thus

makes *s*-SNOM in theory a near-field probe. As a final note to the near-field electromagnetic interaction mechanism, although more complete models have been proposed [22] the physical nature illustrated by the simple model still remains the main results from these complicated models.

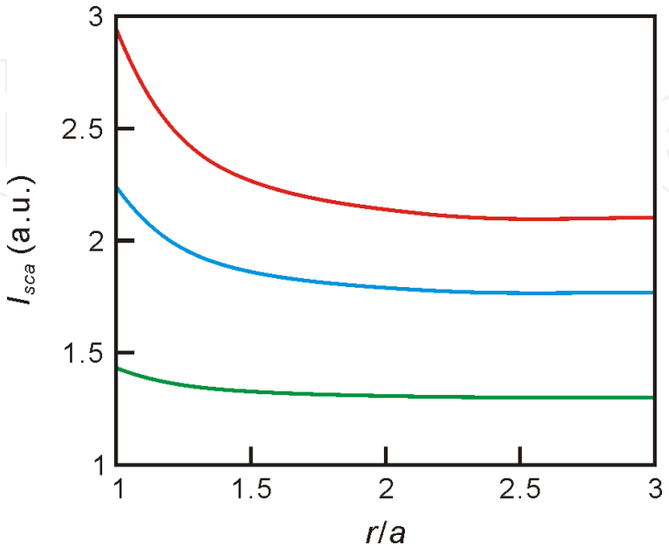

Fig. 3. Calculated scattering intensity, I_{sca}, of near-field interaction between a chromium sphere and three different samples — Au (red line), Si (blue line) and SiO_2 (green line) — *vs.* *z* based on quasi-static dipole model. *r* is the separation between the center of the sphere and the sample surface; *a* is the radius of the sphere.

For a *p*-polarized incident wave, the induced dipole at the sphere has a component normal to the surface, owing to the non-zero field component of the incident wave along the surface normal direction. The induced image dipole is also along the same direction, resulting in an effective polarizability that is larger than α_T. Furthermore, according to Eqs. (1) and (2), α_{eff} reaches the maximal value at $\theta_i = 60^o$ in most cases. Namely, at this incident angle, the scattered radiation is maximized. On the other hand, for an *s*-polarized incident wave, its field component is parallel to the surface, producing a point dipole that also follows the same direction. The image dipole beneath the sample surface is on the other hand along the opposite direction and thus produces a dipole field that counteracts the incident field. Effectively, it partially cancels the dipole above the surface. The resultant effective polarizability in this case is smaller than α_T. That is, the scattered radiation is much smaller than that produced in the case of the *p*-polarized wave excitation. The distinction can be thousand folds difference for a metallic tip [23].

3. Setup of s-SNOM

One major challenge facing the development of *s*-SNOM is how to separate the extremely weak near-field signal originated from the tip apex from the huge background signal originated from the giant scattering radiation from the shaft of the tip and the sample. This is caused by the fact that the illuminated region of the incident optical wave cannot be smaller than the one defined by the diffraction limit. This practical problem was solved by

Wickramasinghe *et al*. [10] and recently by Keilmann *et al*. [14-15]. In their approaches, an interferometric technique combining a dithering tip effectually extracts the weak near-field signal. Taking advantage of the nonlinear dependence of the scattering light field on the tip-sample separation, as shown in Eq. (2), the small variation on the tip-sample separation through the tip dithering or tapping produces many harmonic modulation terms in the scattering light field. While the first harmonic term is dominated by the large background that comes from the scattering from the tip shaft and the sample, the higher harmonic terms contain only the nature of the near-field electromagnetic interaction if the mechanical anharmonicity of the tip-dithering action is put under control [24-25]. The interferometry-based technique has two extra benefits. First, both amplitude and phase can in principle be extracted simultaneously. Second, the weak scattering radiation from the near-field zone can be amplified, which will be manifested below. There are two interferometry-based schemes: homodyne [23, 26] and heterodyne [27]. In the homodyne scheme, a coherent laser beam acts as the excitation light source and the local oscillator simultaneously. As the phase information of the scattering radiation is buried within the detected DC signal, its extraction is not straightforward. In the heterodyne scheme, one part of the laser beam is frequency shifted and, accordingly, the mixed signal between it and the other part is modulating in time, greatly facilitating the phase extraction. The shortcoming is that implementing multiple-wavelength excitation is formidable. The drawbacks of the two schemes have been overcome by pseudoheterodyne [28] and modified heterodyne schemes [29], separately. These interferometric schemes have been developed to extract both the amplitude and phase of the scattering contribution in the near-field region without being interfered by the background scattering [26-31]. Taking advantage of the nonlinear dependence of the scattering light field on the tip-sample separation, as shown in Eq. (2), the small variation on the tip-sample separation through tip dithering or tapping produces many harmonic modulation terms in the scattering light field. While the first-harmonic term is dominated by the large background, the higher-harmonic terms contain only the nature of the near-field electromagnetic interaction if the mechanical anharmonicity of the tip-dithering action is under control [24-25]. Here the modified heterodyne technique is delineated. For the homodyne scheme and its improved version, the authors refer to the publications by Keilmann *et al*. [23].

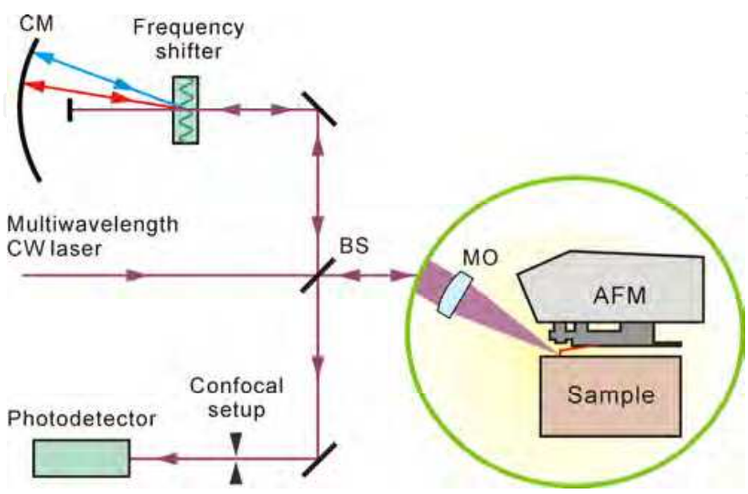

Fig. 4. Optical layout of modified heterodyne *s*-SNOM. BS, beamsplitter; MO, micro-objective lens; CM, curved mirror. Blue and red lines symbolize two excitation wavelengths.

Figure 4 shows the optical layout of modified heterodyne *s*-SNOM that is good for multiple-wavelength excitation. A CW laser – which can be a HeNe laser or a diode-pumped solid-state (DPSS) laser – serves as the coherent excitation light source. The laser beam is first split into two parts by a beamsplitter, BS. The transmitted part, as the excitation beam, is sent to the AFM setup in which a micro-objective lens (MO) focuses it into the tip apex with an incident angle of 60° and the field direction being in the incident plane (*p*-polarized excitation). The scattering radiation is collected backward with the same objective lens. As the AFM tip is dithering at a frequency of ~300 kHz (Ω), the collected scattering radiation is modulating at Ω and its harmonics. The reflected part, as the reference beam, is delivered to a frequency shifter that is an acousto-optical modulator. The diffracted beam that is shifted in frequency by Δ is reflected backward to the frequency shifter to experience another deflection and frequency shifting and thus follows the same path of the incoming beam. With this approach, although the reference beam with a different wavelength would be diffracted at a different angle, it should return back to the same path, without altering the optical alignment. The reference beam then combines with the collected scattering radiation at the beamsplitter. The resultant beam is sent to a high-speed photodetector through a confocal setup that is used to select only the region of the tip apex.

The detected signal by the photodetector is proportional to the square of the combined field of the frequency-shifted reference beam and the collected scattering radiation [27]:

$$\begin{aligned} I_{tot} &\propto \left| E_{ref} \exp\left[i\left(\omega_L - 2\Delta\right)t \right] + E_{sca} \exp\left[i\left(\omega_L + n\Omega\right)t + i\varphi \right] \right|^2 \\ &\propto I_{ref} + I_{sca} + 2\sqrt{I_{ref} I_{sca}} \cos\left[\left(2\Delta + n\Omega\right)t + \varphi \right] \end{aligned}, \tag{6}$$

where I_{sca} is the collected scattering intensity, I_{ref} is the intensity of the frequency-shifted reference beam, ω_L is the laser frequency, n is the harmonic order, and φ is the phase of the scattering radiation with respect to the reference beam. As the total detected signal is composed an AC signal modulated at a frequency of $2\Delta + n\Omega$, a lock-in amplifier referenced to such frequency retrieves the AC component. With the AFM tip is scanned over the sample surface, both I_{sca} and φ are thus retrieved, while the surface topology is simultaneously recorded. The system can be operated in two scanning modes: sample- and tip-scanning modes. In the sample-scanning mode, the sample is scanned by a piezo-driven *xy* stage while the tip is fixed in position. In the tip-scanning mode, the tip is, on the other hand, scanned while the sample is fixed.

4. Extracting near-field images

On the basis of the nonlinear behavior of the near-field interaction with respect to the tip-sample separation, as shown in Eq. (1), it is necessary to place the extracted optical signals of different harmonic orders in scrutiny to verify their exponential-decay dependences on such separation (Fig. 3). Figure 5(a) shows the extracted optical signals of first to fourth harmonic orders as a function of the tip-sample separation from a gold surface with nanometer-scaled gold particles. The scattering signal drops almost exponentially with the tip-sample separation, signifying the recorded third and fourth-harmonic signals are generated in near field. A fit of the fourth-harmonic signal to an exponential decay curve gives a decay length of 10 nm, reflecting the short-range electromagnetic interaction between the tip and the

sample illustrated by Eq. (1) and demonstrating the near-field nature of the high harmonic-order signals. Figure 5(b) shows the topography image of rough Au coated silicon surface. The prominent features of this image show one-to-one correspondence with the images of the scattering optical signals of the second to fourth harmonic orders, as shown in Figs. 5(c) to (e). The interference-like ripples in Fig. 6(c) is an artifact that could be caused by the interference between the scattering light wave of the tip shaft and that of the sample, as similarly observed previously [23]. This assignment is because a slight nonlinear mechanical response of the tip dithering motion at a frequency of Ω provides a certain amount of sinusoidal component at 2Ω that then introduces some harmonic contribution at 2Ω into the elastic scattering optical signal from the tip shaft. That trait is also manifested itself in its non-decay dependence on the tip-sample separation, z, shown in Fig. 5(a), which is a direct evidence of the non-near field scattering contribution by the tip shaft.

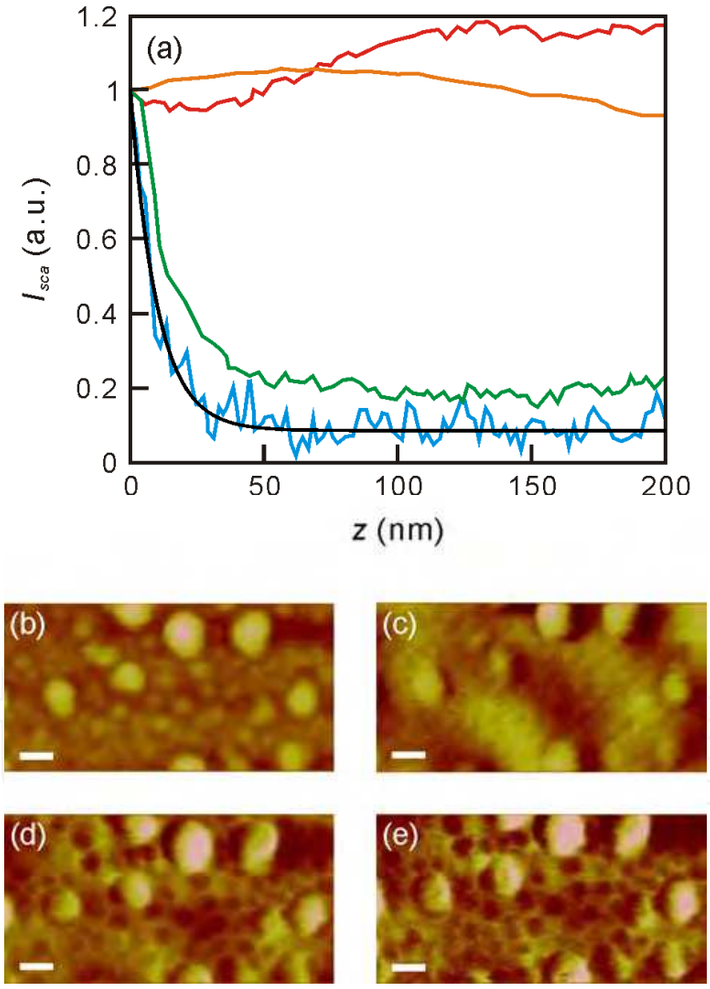

Fig. 5. (a) Collected *s*-SNOM signals of 1st (orange line), 2nd (red line), 3rd (green line), and 4th (blue line) harmonic orders on Au surface as a function of tip-sample separation, z; Scanned images of topography (b) and *s*-SNOM signal of 2nd (c), 3rd (d), and 4th (e) harmonic orders. Scale bars represent 100 nm. The black solid line is the fit to an exponential decay. The excitation wavelength is 632.8 nm.

Two more facts can be extracted from the near-field images of 3rd and 4th harmonic orders, shown in Figs. 5(d) and (e), are worthy of further discussion. Firstly, the near-field optical signal observed on large Au nanoparticles (diameter > 200 nm) is larger than that observed on small ones (diameter < 100 nm). This may be originated from the fact that the observed scattering signal from the tip-sample system can be enhanced by its plasmon resonance character [32]. As the plasmon resonance wavelength of a small Au nanoparticle is shorter than that of a large Au nanoparticle and thus is further away from the excitation wavelength of 632.8 nm [33], the corresponding effective polarizability for the small nanoparticle can be smaller than that for the large nanoparticle. Secondly, enhanced scattering signal is evident in the gap between these particles, which can be attributed to the following two causes. On the one hand, the gap mode existing between the two adjacent nanoparticles [34] induces localized strong field within and thus enhances optical scattering. The resonance wavelength of the gap mode is, on the other hand, red shifted and is closer to the excitation wavelength, thus increasing the corresponding effective polarizability and also enhancing the scattering radiation. These factors must be accounted for the interpretation of the extracted near-field images with the use of the excitation wavelength close to the electromagnetic resonance of the tip and the sample under scrutiny.

As to the geometry of the *s*-SNOM setup shown in Fig. 4, there are several advantages for such side-illumination geometry. In sum, except for the better laser excitation and signal collection efficiencies (60^{o} incident angle and *p*-polarization excitation), the sample needs not be transparent. In contrast, for *s*-SNOM with a transmission-illumination geometry – in which the excitation laser beam illuminates the tip apex through the sample and along the tip shaft, transparent samples are must and furthermore a special polarization configuration is prepared for the excitation beam to enhance the field component at the tip apex along the tip shaft [35-37]. Nevertheless, for the side-illumination geometry, the cantilever that holds the tip shaft cannot obstruct the excitation laser beam from irradiating the tip apex. Namely, the tips must protrude from the front side of the cantilever. As a consequence, this geometry entails special AFM tips allowing for side illumination (such as AdvancedTEC tips from Nanosensor, Olympus Probes, Visible Apex tips from Bucker, etc.) or conventional tips modified by focused-ion beam.

Lastly, two differing considerations in choosing the tip material are given to the use of *s*-SNOM in probing local dielectric property and extracting local field. For the first application, the material under study is in general not near electromagnetic resonance with the incident optical wave, for which the scattering signal from the near-field interaction between the tip and the sample is often very weak. To enhance the scattering signal, the tip is preferably made by metal (silver or gold) that bears plasmon resonance with respect to the excitation laser beam. Equations (1) and (3) show that the resultant scattering signal can thus be amplified by the use of such metal tip. As the conventional AFM tips are made with the application of high precision etching process on crystalline silicon and silicon nitride, the shape of the tip apex can thus be controlled down to sub-20 nm scale. Coating of single or multiple layers of metals through thermal deposition can be applied to the tip to create a special dielectric property that is suitable for near-field applications [38]. The thickness of the coating has to be larger than the skin depth of the metal coating at the excitation wavelength to avoid the effect by the underneath tip material. However, silver and gold often tend to aggregate in tens of nanometer on the tip surface [39], creating non-continuous coating and thus bearing unstable optical response. Meticulous control in the metal coating

process is necessity to increase its production yield. The resonance wavelength of a silver coated tip is about 450 nm while that of a gold one is about 600 nm. For such reason, the silver-coated tip is often used with the excitation wavelengths shorter than 600 nm, while the gold-coated tip is with the wavelengths longer than 600 nm. Furthermore, silver has a smaller optical loss than gold, but it can oxidize or sulfurize in ambient condition, altering its optical property in time. On the other hand, gold is rather stable in air, while it is softer than silver and thus does not endure during scanning probe operation. One has to place such factors into account while choosing tip coating for *s*-SNOM. For the applications of retrieving local field, the disturbance by the tip has to be minimized as much as possible. For such reason, the electromagnetic resonance of the tip needs to be avoided and therefore silicon or silicon nitride tips are commonly used directly. This is so because their electromagnetic resonance wavelengths are distant from the visible wavelength range. One concern has to be placed in the use of silicon tips. As silicon oxidizes in air, a thin silicon oxide coating (1-2 nm) can modify the optical response with respect to the excitation laser beam considerably, accordingly diminishing the scattering signal [38].

5. Spatial resolution

The resolution of *s*-SNOM by its operating principle depends on the size and the shape of the tip apex. In Fig. 5 above, the near-field amplitude image of the 4th harmonic order of the tip dithering frequency shows a one-to-one correspondence with the topography image. This match reflects that the spatial resolution of the recorded near-field image is comparable to that of the topography image. That is, the lateral resolution is at least 5 nm that is greatly dependent on the tip apex. On the other hand, the fit of the *s*-SNOM signal of the 4th harmonic order as a function of the tip-sample separation, Fig. 5(a), shows that it follows an exponential decay with a decay length of 9.8 nm. This result is an evidence for the vertical resolution of *s*-SNOM. Similar to other scanning probe microscopic techniques, many other factors can have great influences on the spatial resolution. Besides the tip shape – specifically the radius of the tip apex, the dielectric property of the sample under study and the geometric structure of the sample in vicinity of the tip apex are anticipated to play two additional key roles in *s*-SNOM on the basis of the tip-sample near-field interaction. Such considerations are worthy of further exploration.

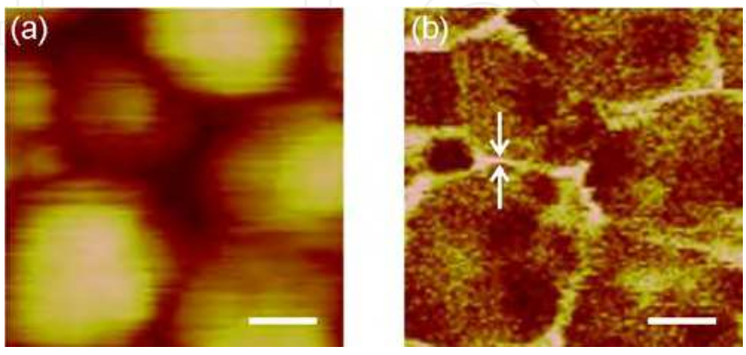

Fig. 6. Scanning topography (a) and *s*-SNOM optical amplitude (b) images of silver nanoparticle array embedded in anodic aluminum oxide. The gap between two counter-pointing arrows indicates the region where strong intensity resides. Scale bars represent 40 nm.

The following two examples illustrate how the field interaction and the geometric factors around the tip influence the spatial resolution of *s*-SNOM. The first sample is an array of silver nanoparticles embedded in aluminum oxide matrix. The silver nanoparticles were electrodeposited into a two-dimensional hexagonal ordered nanochannel array that was formed during anodization of smooth aluminum foil [40]. The gap between adjacent nanoparticles is about 5 nm and confirmed by electron microscopy. Figure 6 shows its topography and near-field intensity amplitude images recorded with a silicon tip with a radius of curvature of less than 10 nm. Notice that the close examination of the two images shows that a large intensity extends for ~6 nm between adjacent nanoparticles. In this observation, the nanoparticle array with a specific interparticle spacing serves as a ruler and confirms the lateral resolution of this *s*-SNOM measurement. An *s*-SNOM image of aggregated gold nanoparticles were reported previously [32] to portray the coherently oscillating nature of plasmon resonant of individual nanoparticles, expect that no confirmation of the gap by other means was provided. As an example, using a carbon nanotube attached on a silicon tip, Hillenbrand and his workers successfully recorded both amplitude and phase images of gold nanoparticles with a good spatial resolution, though no direct proof by electron microscopy was given [41]. The second example is a square array of annular trenches on a gold film of 200 nm thickness. These carved rings were made by focused ion beam. The diameters of the inner and outer circles are 250 and 330 nm, respectively; the depth is 200 nm; the spacing between adjacent rings is 600 nm. Figure 7 shows the topology and near-field amplitude scanned with sharp and blunt PtIr5-coated

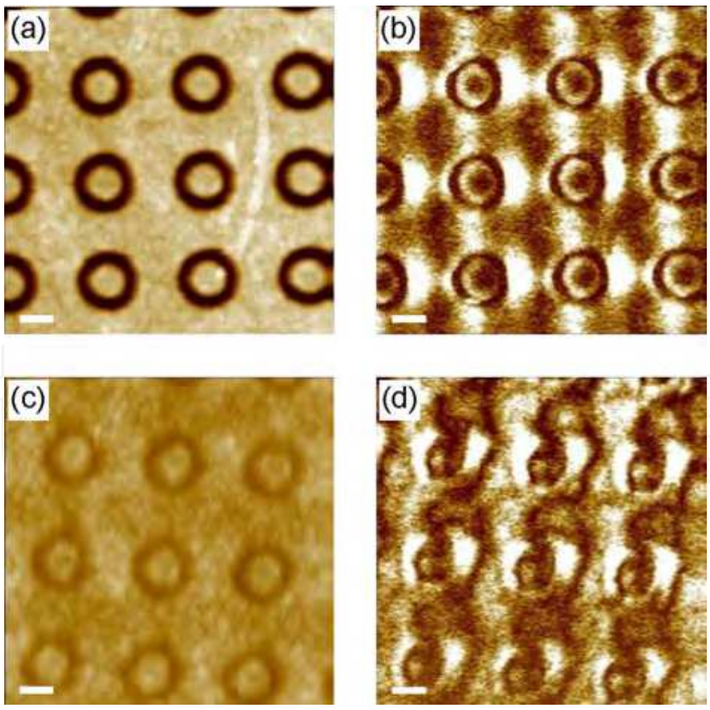

Fig. 7. Topology images of annular trench array on gold film made by focused ion beam recorded with (a) sharp and (c) blunt tips and their corresponding intensity amplitude images, (b) and (d), respectively. The diameters of the inner and outer circles are 250 and 330 nm, respectively. Scale bars represent 200 nm.

silicon tips. The recorded near-field amplitude image – Fig. 7(a) – with the sharp tip shows a good correspondence with the corresponding topology image – Fig. 7(b) – that reflects the examination with scanning electron microscopy. In contrast, the use of the blunt tip blurs the resultant topology image – Fig. 7(c) – and creates a peculiar near-field amplitude image – Fig. 7(d) – that is quite distinct from the one obtained with the sharp tip.

6. Applications in nanomaterials

In the sphere of nanomaterials, manifold materials are architecturally configured with nanometer-scale precision, aiming for specific and contingent, multiplex while coherently collaborative functions. It is requisite to comprehend their structural arrangement through innovative material processing methods and, even furthermore, their inter-correlated properties directly. The demonstration of *s*-SNOM being capable of resolving dielectric characteristic of surface in nanometer scale exemplifies one prototypical case. At first, such effort entails a sample that is made of distinct materials with known dielectric constants. Fischer's pattern [42] is chosen here to serve as the first example. Such pattern is made with the following nanosphere lithography procedure. First, polymethylmethacrylate (PMMA) spheres of 300 nm in diameter are self assembled into a hexagonal closely packed pattern on a silicon surface. Second, gold is thermally deposited to overlay such pattern with a gold film of 50 nm in thickness. Finally, the sample is immersed in an acetone solution to remove the PMMA spheres, yielding a hexagonal array of triangular gold disks. Some PMMA residues remain in the vicinity of the gold disks owing to incomplete dissolution of PMMA spheres. The resultant pattern sample thus bears three differing materials (silicon, gold and PMMA) that represent archetypal semiconductor, metal and polymer. The AFM topography image, shown in Fig. 8(a), only shows such hexagonally packed pattern devoid of material composition. In contrast, the scanned image of the scattering intensity of the third-harmonic order, $I_{sca}(3\Omega)$, is shown in Fig. 8(b) and clearly portrays three regions with distinct scattering intensities: triangular areas with the highest signal, round areas with a medium signal and peripheral areas surrounding the triangular areas with the smallest signal. The correspondence with the simultaneously recorded topography image suggests that the brightest areas stand for gold, the less bright areas signify silicon and the dimmest areas are indicative of PMMA. Such assignment can be confirmed with the quantitative comparison of their relative intensities with respect to the calculation according to the quasi-static dipole model, Eqs. (1)-(5). Figure 8(c) displays the calculated $I_{sca}(3\Omega)$ as a function of the real part of the dielectric constant of the sample, Re(ε). The measured scattering intensities of the three areas are also plotted in the figure according to the dielectric constants of the assigned materials. The experimental data points agree with the calculated values, if the imaginary part of the dielectric constant, Im(ε), is assumed to be -0.1 that is valid for these three lossless materials at 632.8 nm. This correspondence demonstrates the exploitation of *s*-SNOM to extract local dielectric property within sub-10 nanometers. The dielectric constant of material contains Lorentz and Drude contributions. The former one represents local oscillators coming from electronic and vibrational transitions, while the latter one reflects the influence of free carriers. Huber *et al.*, via taking advantage of the variation of the Lorentz contribution, used *s*-SNOM, operating at 10.7 μm, to resolve different materials of tungsten, aluminum, silicon and silicon oxide on the polished cross section of a pnp transistor [43]. More recently, they mapped the doping concentration distribution of a

silicon transistor [44] with a resolution of 40 nm at 2.54 THz by the use of the Drude contribution: the carrier concentration influences the plasma contribution of the dielectric constant of silicon, yielding visible contrast to resolve the regions of different doping concentrations. This approach of recording local electrical property is non-contact and is better than the contact counterparts, such as surface capacitance microscopy, that often acquire interference results owing to electrical contact.

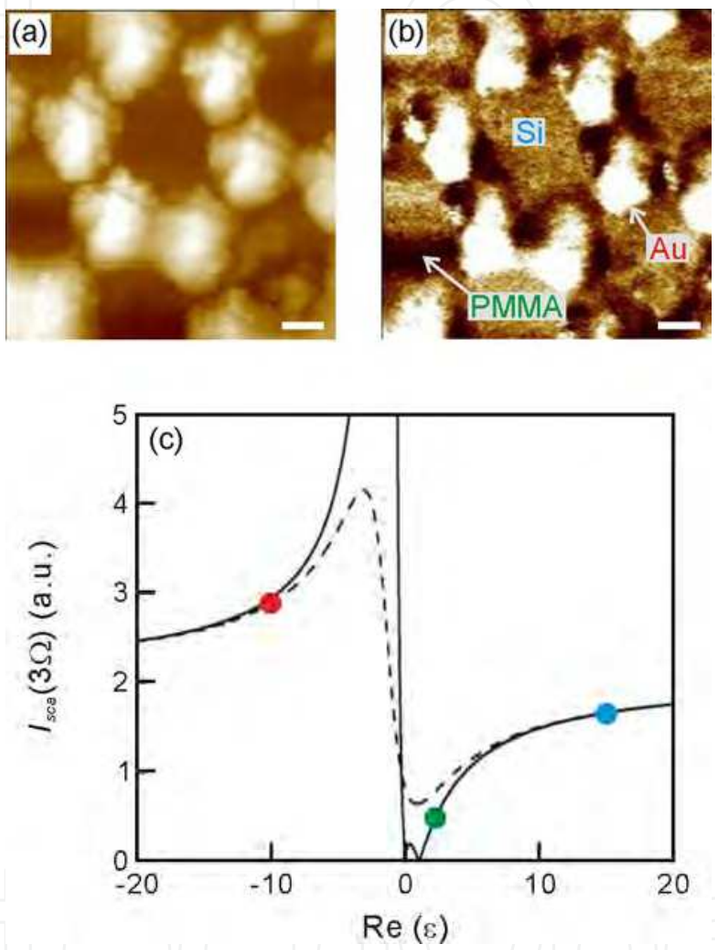

Fig. 8. Images of (a) topography and (b) near-field amplitude of the third-harmonic order, $I_{sca}(3\Omega)$, of a Fischer's pattern [10] excited at 632.8 nm; (c) comparison between calculated $I_{sca}(3\Omega)$ as a function of the real part of the dielectric constant of the sample, Re(ε), with the imaginary-part values of -0.1 (solid line) and -10 (dashed line) and measured values extracted from the corresponding regions of Si (blue dot), PMMA (green dot) and Au (red dot) in (b). Scale bars represent 100 nm.

The capability of resolving local dielectric property with *s*-SNOM has been utilized by us to examine nanometer-scale optical contrast of the phase-change layer of blue-ray recordable and erasable disks [45]. The quality of recording or reading data is greatly dependent on the detailed variation of optical characteristics within the recorded mark that is within 150 nm in size. Fast temperature quenching induces amorphous phase, while slow temperature

cooling yields polycrystalline. The optical signature within such mark is not discernible with conventional aperture-typed SNOM owing to its >50 nm resolution, but would be possible with high-resolution *s*-SNOM. The near-field image of the AgInSbTe phase-change layer of a blue-ray disc obtained by the *s*-SNOM is shown in Fig. 9(a). The recorded marks are revealed by the prominent near-field optical contrast. According to the dielectric constants of crystalline and amorphous AgInSbTe at 632.8 nm (3.63+*i*21.2 and 8.14+*i*9.35, respectively) [46], the ratio between the calculated tip-induced scattering intensities of the crystalline and amorphous phases is 1.28 that that is very close to the experimentally determined value of 1.30. This observation indicates that the dark regions along the protruding track in Fig. 9(a) are amorphous AgInSbTe created during the recording process. This inference agrees with TEM observation. The scattering intensity profile of the recorded disc shows that the marks have the minimum width of ~160 nm by measured the cross section (dash lines), while no such feature is present in the non-recorded disc, shown in Fig. 9(b). Such prominent marks are not recognizable in the corresponding topographic image. In addition, 30-nm isolated crystalline domains within the amorphous recorded mark emerge in Fig. 9(a) and also were

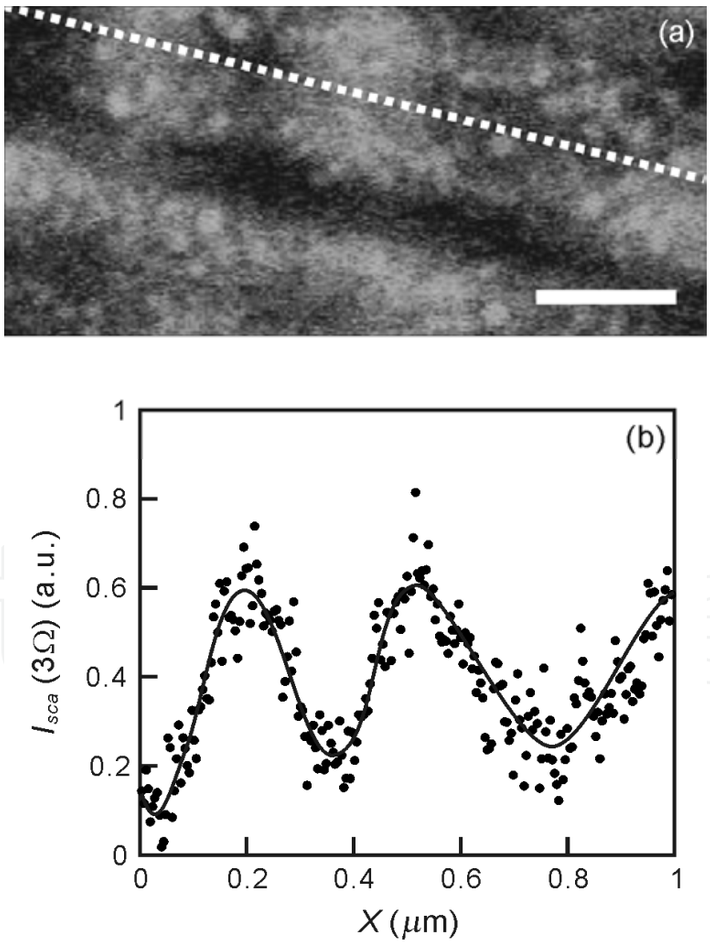

Fig. 9. (a) Image of the scattering intensity of third-harmonic order of BD-RE disc; (b) intensity profile along the track, marked by the dashed line in (a). Scale bar represents 200 nm.

observed by TEM measurement. This nanometer-scaled optical signature could potentially deteriorate the carrier-to-noise ratio in reading this optical storage medium. On the other hand, the studies of BD-RE with conductive AFM [47-48] only presented either conducting or non-conducting state of the phase-change layer, thus prohibiting from using this technique to investigate the intricate phase-change characteristics within the recorded marks. Compared with the result obtained with aperture-typed SNOM by Yoo and coworkers [50], its spatial resolution is not enough to extract the detailed variation, including the nanometer-scaled features within the recorded marks.

7. Applications in nanophotonics

In the sphere of nanophotonics, the energy of electromagnetic field is concentrated or controlled with some specially prepared nanostructures beyond the limit set by traditional optical theory where the optical mode density – on which the principles of optics rely – in the region of interest is assumed as in free space or only slightly perturbed from it. In contrast, the optical mode density in the content of nanophotonics has drastically distinct distribution that is governed by the nanostructured materials in proximity. Because of such distinct optical mode density, its understanding and therefore control are limited by itself that is beyond the traditional optical theory. Moreover, transferring its information content to our macroscopically sensible realm is also influenced greatly by such limitation, entailing unconventional experimental means to truthfully convey the optical information. The *s*-SNOM is representative of one of such many innovative techniques. According to Eq. (5), the scattering intensity induced by the tip-sample near-field interaction is also dependent on the field in the vicinity of such tip-sample complex. Specifically, the scattering radiation can be induced upon the presence of certain surface electromagnetic field. Surface plasmon wave (SPW) exemplifies such surface electromagnetic field, by which the evanescent wave propagates on the metal-dielectric or metal-vacuum interface [29, 43, 50]. In this section, the near-field characteristics of the SPW emanating from single hole or hole arrays of nanometer size made by focused ion beam on metal film are present.

The first example is single hole of 150 nm in diameter on a silver film of 200 nm in thickness. Figure 10 schematically shows the application of *s*-SNOM to such sample. In the case like that, three scattering field contributions are present in the thus obtained *s*-SNOM images. The first contribution is the outcome of the interaction between the incident wave and the tip apex that is in vicinity of the sample surface, producing the first scattering field, E_1. The second contribution is made by the SPW induced by the interaction of the incident wave and the hole. The thus induced SPW propagates to the tip apex, producing the second scattering field, E_2. The third contribution is made the SPW induced by the tip apex that is approached to the sample surface, which propagates to the hole, reflects back to the tip apex, and gives the third scattering field, E_3. The wave vector, $\boldsymbol{k}_{SPW}$, this surface plasmon wave follows the following dispersion relation, $\left|\boldsymbol{k}_{SPW}\right| = \left|\boldsymbol{k}_0\right| \cdot \sqrt{\varepsilon_1 \varepsilon_2 / (\varepsilon_1 + \varepsilon_2)}$ [51], where $\boldsymbol{k}_0$ is the wave vector of the incident wave, and ε_1 and ε_2 is the dielectric constants of vacuum and silver, respectively. The detailed derivation of the resultant scattering wave as well as the corresponding one in inverse space is given in Ref. 50 and is not repeated here. According to the derived results, the interference between E_1 and E_2 produces two $\left|\boldsymbol{k}_{SPW}\right|$-radius circles centered at $\pm\left|\boldsymbol{k}_0\right|\sin\theta_i$. Furthermore, the interference between E_1 and E_3

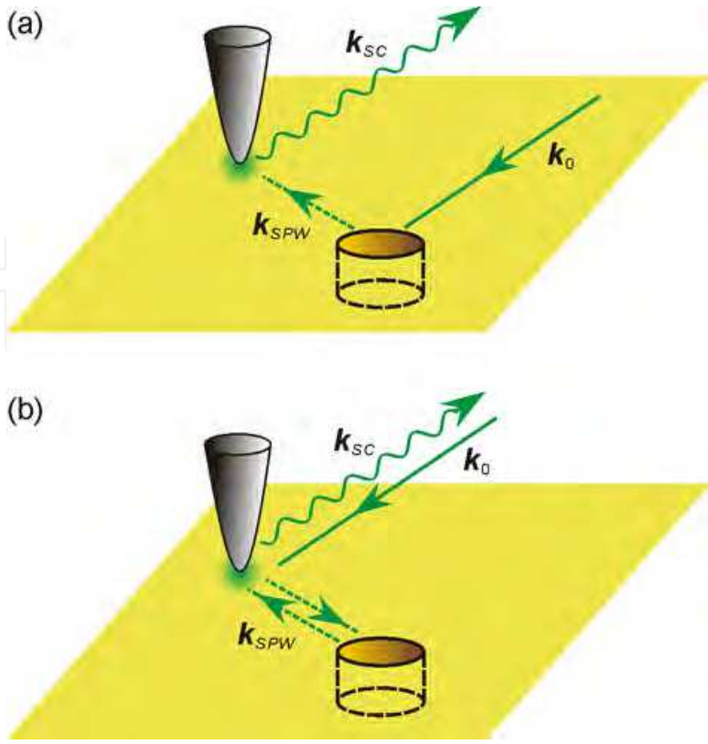

Fig. 10. Two scattering field contributions of surface plasmon waves generated from nanohole (a) and tip (b) during *s*-SNOM scanning of a circular hole on gold film. $\boldsymbol{k}_0$, the wave vector of the incident light wave; $\boldsymbol{k}_{SC}$, the wave vector of the scattering light wave; $\boldsymbol{k}_{SPW}$, the wave vector of the surface plasmon wave.

produces one $2|\boldsymbol{k}_{SPW}|$-radius circle centered at origin. Such prediction is confirmed with the scanned intensity amplitude image of such sample, shown in Fig. 11. Notice that the intensity amplitude image, shown in Fig. 11(a), exhibits rather complex ring-like pattern around the nanohole. After performing fast Fourier transform (FFT), three circles emerge in the *k*-space image, Fig. 11(b), and match with the theoretical prediction above, supporting the interpretation of near-field images obtained by *s*-SNOM. The schematic diagram of the image in *k*-space is shown in Fig. 11(c). To further support the interpretation of the near-field amplitude image of single nanohole discussed above, numerical calculation based on finite-difference time-domain (FDTD) method was performed. The simulation, without considering the tip, was executed over a region of 16.8 μm × 12.8 μm with a mesh size of 20 nm and the dielectric function of silver was taken from Ref. 52. A Gaussian beam with a 4-μm waist was used to simulate the experimental condition. The calculated distribution of the field component normal to the surface in *k*-space only two $|\boldsymbol{k}_{SPW}|$-radius circles, because the third contribution of the scattering field is induced by the tip apex and was not considered in the calculation. By removing the large circle of the recorded near-field image and subsequently transforming it back to *r* space, the resultant *r*-space image matches almost perfectly with the calculated result [50]. This consistency thus supports the theoretical analysis of the Fourier-transformed image above. Finally, the single-nanohole study above therefore demonstrates that examining near-field images in *k* space helps to identify the origins of different surface plasmon waves, allowing for in-depth investigation

of the fundamental nature of surface electromagnetic waves that may exist around nanostructures [53]. The *k*-space examination can also be applied to ordered hole arrays and has been delineated in Ref. 50. For such case, each hole in the array has both E_2 and E_3 components, while only one E_1 is attributed to the tip apex. The resultant E_2 and E_3 are given by the sum of individual holes. Assuming that two successive scattering events is neglected because of the propagating loss of SPW, the total scattering field in *k*-space can be similarly derived [50], conferring a *k*-space pattern of the near-field image of the nanohole array that is the product of the *k*-space pattern of single nanohole and the structure factor $S(\boldsymbol{k}) = \sum_{m,n} \exp\left(ik_x ma + ik_y na\right)$. The corresponding Fourier-transformed images in *k* space obtained from the experimental data match very well with the predicted patterns [53]. One important implication emerges from this study. In the near-field study of surface plasmon polaritons with *s*-SNOM, the tip apex always acts as the plasmon inducer as well, making the resultant near-field images rather complicated. Performing Fourier analysis on the recorded near-field images facilitates the identification of the tip-induced contribution, setting a solid foundation for in-depth examination of the fundamental nature of surface plasmon polaritons.

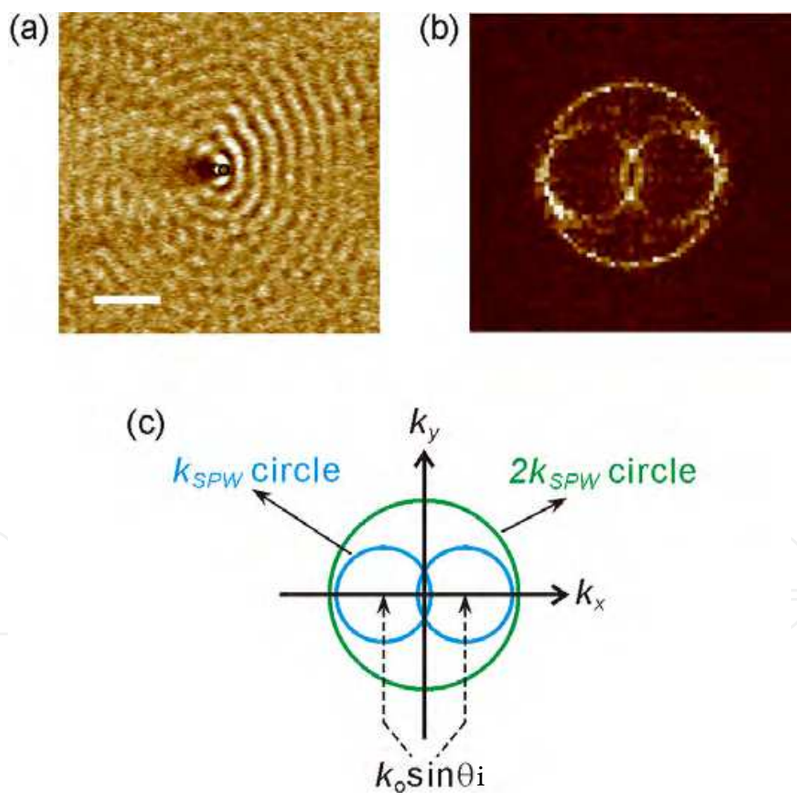

Fig. 11. (a) Scattering amplitude image and (b) Fourier transformed image single nanohole on gold film; (c) schematic Fourier-transformed image of different contributions. The hole diameter is 150 nm and the excitation wavelength is 532 nm. The hole is marked as open black circle. The scale bar represents 1 μm. k_0, wave vector of incident optical wave; k_{SPW}, wave vector of surface plasmon wave.

The aforementioned ordered hole arrays made on a metallic film can exhibit enhanced or suppressed optical transmission through such corrugated films at specific wavelengths [54]. Many applications, such as color filters, sensitive biodetectors based on fluorescence on such films, etc., have been projected. It has been proposed and experimentally verified that such anomalous properties are originated from the launching of SPW upon the excitation of an incident optical wave at those particular wavelengths [55], while examining such plasmon wave in high resolution is not made possible with conventional aperture-type SNOM. Figure 12 presents a closer view of topographic, near-field optical intensity and phase images on the edge of a square circular hole array. Notice that the SPW outside the array is constructed coherently by those emitting from individual holes and propagates away from the array, shown in Figs. 12(a) and (b), as the incident wavelength meets the criterion for exciting surface plasmon wave of an ordered array:

$$\left|\boldsymbol{k}_0\right|\sin\theta_i\left(\cos\varphi\hat{\boldsymbol{x}}+\sin\varphi\hat{\boldsymbol{y}}\right)-\boldsymbol{k}_{SPW}=\frac{2\pi}{a}\left(m\hat{\boldsymbol{x}}+n\hat{\boldsymbol{y}}\right),\ \left(m,n=0,\pm1,\pm2,\cdots\right), \tag{7}$$

where φ is the azimuthal angle of $\boldsymbol{k}_0$ on the surface. If the incident wavelength is off the excitation condition, no such coherently constructed plasmon wave emanates from the edge of the hole array, shown in Figs. 12(c) and (d). The interior magnified near-field amplitude and phase images of a square elliptic hole array are shown in Figs. 12(f) and (g). In this case, the surface component of the incident light wave, $\boldsymbol{k}_{0,//}=\boldsymbol{k}_0-\left|\boldsymbol{k}_0\right|\cos\theta_i\hat{\boldsymbol{z}}$, is perpendicular to the long axis of the elliptic holes – $\hat{\boldsymbol{l}}$ (i.e., $\boldsymbol{k}_{0,//}\perp\hat{\boldsymbol{l}}$). As shown in Fig. 12(f), the regions of the localized field distribution manifest as the bright crescents located around the rim of the elliptical holes. This agrees with the expectation of the excitation of localized surface plasmon. In the corresponding phase image shown in Fig. 12(g), a 180° phase change takes place from the left crescent to the right crescent of the hole. The interpretation of these near-field results relies on the understanding that *s*-SNOM probes the field component normal to the surface in the present polarization configuration [29]. The two experimental observations above therefore indicate the nature of strong dipole oscillating field along the short axis of the elliptical hole – $\hat{\boldsymbol{s}}$. This interpretation agrees with two additional facts in Fig. 12: no vertical field component is observed and the phase appears randomly inside the hole. These results thus reflect the excited localized surface plasmon in the case that $\boldsymbol{k}_{0,//}\perp\hat{\boldsymbol{l}}$. In contrast, no dipole-like oscillating feature appears in the near-field images in the case that $\boldsymbol{k}_{0,//}\perp\hat{\boldsymbol{s}}$, reflecting weak plasmon excitation. A calculation result based on finite-different-time-domain method further confirms this interpretation [56].

8. Conclusions

In this chapter, we present a high-resolution near-field microscope – scattering-type SNOM (*s*-SNOM). Its basic operation principle is based on the near-field electromagnetic interaction between a scanning tip and the sample of interest. An interference-based heterodyne detection scheme is employed to extract both amplitude and phase of the extremely weak scattering radiation from the tip-sample complex. The local dielectric property of the sample – if the excitation wavelength is within the resonant excitation condition of the tip apex, and the local surface electromagnetic field – if the excitation wavelength is outside the resonance wavelength range of the tip apex, are readily extracted with this techniques. Considerations while exploiting such unique functions are discussed in detail. A few cases are presented to

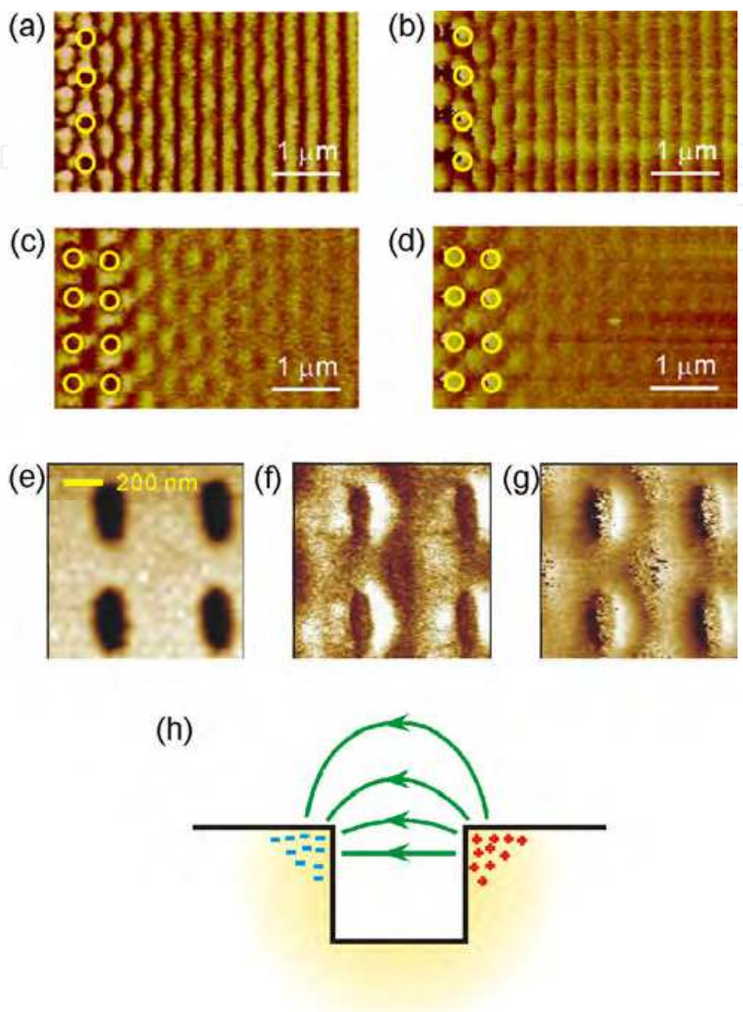

Fig. 12. Near-field intensity and phase images of a circular hole array with two excitation wavelengths (λ_{ex}). (a) Intensity and (b) phase images for λ_{ex} = 532 nm; (c) Intensity and (d) phase images for λ_{ex} = 632.8 nm. The yellow circles indicate the hole position. Topographic (e), near-field optical intensity (f) and phase images (g) around the rim of elliptical hole arrays with *s*-polarization excitation; (h) schematic cross-sectional view of charge distribution and electric force lines of a dipole oscillation.

exemplify these unique characteristics of this new-generation near-field microscopic technology. In particular, the extraction of local composition of the recorded marks of the phase-change layer of blue-ray recordable and erasable disks is presented. ~10-nm optical signatures within such recorded marks are identified and are correspondent to crystalline

domains that are barely visible to high-resolution transmission electron microscopy. Furthermore, surface plasmon waves are revealed with *s*-SNOM and the effect caused by the tip on the acquired near-field images is carefully examined. The analysis in *k*-space domain successfully resolves this effect. The application of *s*-SNOM to nanomaterials and nanophotonics is still young. One can expect that its exploitation in these realms and even beyond can be furthered more so in near future.

9. References

[1] M. Born and E. Wolf, Principle of Optics (Cambridge university Press, UK, 1999).
[2] B. Hecht, B. Sick, U. P. Wild, V. Deckert, R. Zenobi, O. J. F. Martin and D. W. Pohl, *The J. of Chem. Phys.*, 112, 7761 (2000).
[3] *Near-Field Nano/Atom Optics and Technology*, edited by M. Ohtsu (Springer-Verlag, Berlin, 1998).
[4] D. Courjon, *Near-Field Microscopy and Near-Field Optics* (Imperial College Press, London, 2003).
[5] J. W. P. Hsu, *Mater. Sci. Engineer.*, 33, 1 (2001).
[6] E. H. Synge, *Philos. Mag.*, 6, 356 (1928).
[7] D. W. Pohl, W. Denk and M. Lanz, *Appl. Phys. Lett.*, 44, 651 (1984).
[8] A. Lewis, M. Isaacson, A. Harootunian and A. Muray, *Ultramicroscopy*, 13, 227 (1984).
[9] H. A. Bethe, *Phys. Rev.*, 66, 163 (1944).
[10] F. Zenhausern, Y. Martin, and H. K. Wickramasinghe, *Science*, 269, 1083 (1995).
[11] *Nano-Optics and Near-Field Optical Microscopy*, edited. by A. Zayats and D. Richard (Artech House, Boston, 2009)
[12] M. B. Raschke and C. Lienau, *Appl. Phys. Lett.*, 83, 5089 (2003).
[13] J. E. Hall, G. P. Wiederrecht, S. K. Gray, S. -H. Chang, S. Jeon, J. A. Rogers, R. Bachelot, and P. Royer, *Opt. Express*, 15, 4098 (2007).
[14] L. Gomez, R. Bachelot, A. Bouhelier, G. P. Wiederrecht, S. H. Chang, S. K. Grey, F. Hua, S. Jeon, J. A. Rogers, M. E. Castro, S. Blaize, I. Stefanon, G. Lerondel, and P. Loyer, *J. Opt. Soc. Am. B*, 23, 823 (2006).
[15] F. Keilmann, *Journal of Electron Microscopy*, 53, 187 (2004).
[16] M. I. Stockman, *Phys. Rev. Lett.*, 93, 137404-1 (2004).
[17] S. Patane, P. G. Gucciardi, M. Labardi, and M. Allegrini, Riv. Nuovo Cimento 27, 1 (2004).
[18] R. Hillenbrand, B. Knoll and F. Keilmann, *Journal of Microscopy*, 202, 77 (2000).
[19] B. Knoll and F. Keilmann, *nature*, 399, 134 (1999).
[20] C. F. Bohren, and D. R. Huffman, *Absorption and Scattering of Light by Small Particles* (Wiley, 1998).
[21] C. Meixner and P. R. Antonicwcz, Phys. Rev. B 13, 3276 (1976).
[22] A. Cvitkovic, N. Ocelic and R. Hillenbrand, *Opt. Express*, 15, 8550 (2007).
[23] F. Keilmann, and R. Hillenbrand, *Phil. Trans. R. Soc. Lond. A*, 362, 1 (2004).
[24] R. Hillenbrand, M. Stark and R. Guckenberger, *Appl. Phys. Lett.*, 76, 3478 (2000).
[25] A. Bek, R. Vogelgesang and K. Kern, *Appl. Phys. Lett.*, 87, 163115 (2005).
[26] B. Knoll and F. Keilmann, *Opt. Commun.*, 182, 321 (2000).
[27] F. Keilmann and R. Hillenbrand, *Phys. Rev. Lett.*, 85, 3029 (2000).
[28] N. Ocelic, A. Huber and R. Hillenbrand, *Appl. Phys. Lett.*, 89, 101124 (2006).

[29] J. Y. Chu, T. J. Wang, Y. C. Chang, M. W. Lin, J. T. Yeh, and J. K. Wang, *Ultramicroscopy*, 108, 314 (2008).
[30] M. B. Raschke, L. Molina, T. Elsaesser, D. H. Kim, W. Knoll and K. Hinrichs, *ChemPhysChem*, 6, 2197 (2005).
[31] Z. H. Kim, B. Liu and S. R. Leone, *J. Phys. Chem. B*, 109, 8503 (2005).
[32] Z. H. Kim and S. R. Leone, *Opt. Express*, 16, 1733 (2008).
[33] S. A. Maier, *Plasmonics: Fundamentals and Applications* (Springer-Verlag, Berlin, 2007).
[34] H. H. Wang, C. Y. Liu, S. B. Wu, N. W. Liu, C. Y. Peng, T. H. Chan, C. F. Hsu, J. K. Wang and Y. L. Wang, *Adv. Mat.*, 18, 491 (2006).
[35] R. Laddada, P. M. Adam, P. Royer and J. L. Bijeon, Opt. Eng., 37, 2142 (1998).
[36] G. P. Wiederrecht, *Eur. Phys. J. Appl. Phys.*, 28, 3 (2004).
[37] V.N. Konopsky, *Opt. Commun.*, 185, 83 (2000).
[38] D. Haefliger, J. M. Plitzko, and R. Hillenbrand, *Appl. Phys. Lett.*, 85, 4466 (2004).
[39] R. Gupta, M. J. Dyer, and W. A. Weimer, *J. of Appl. Phys.*, 92, 5264 (2002).
[40] A. P. Li, F. Muller, A. Birner, K. Nielsh and U. Gosele, *J. of Appl. Phys.*, 84, 6023 (1998).
[41] R. Hillenbrand, F. Keilmann, P. Hanarp, D. S. Sutherland and J. Aizpurua, *Appl. Phys. Lett.*, 83, 368 (2003).
[40] H. H. Wang, C. Y. Liu, S. B. Wu, N. W. Liu, C. Y. Peng, T. H. Chan, C. F. Hsu, J. K. Wang and Y. L. Wang, *Adv. Mat.*, 18, 491 (2006).
[41] A. J. Huber, F. Keilmann, J. Wittborn, J. Aizpurua, and R. Hillenbrand, *Nano lett.*, 8, 3766 (2008).
[42] U. C. Fischer, J. Heimel, H. J. Maas, M. Hartig, S. Hoeppener and H. Fuchs, *Surf. Interface Anal.*, 33, 75 (2002).
[43] A. Huber, D. Kazantsev, F. Keilmann, J. Wittborn, and R. Hillenbrand, Adv. Mater. 19, 2209 (2007).
[44] A. J. Huber, F. Keilmann, J. Wittborn, J. Aizpurua, and R. Hillenbrand, *Nano lett.*, 8, 3766 (2008).
[45] J. Y. Chu, S. C. Lo, S. C. Chen, Y. C. Chang, and J. K. Wang, *Appl. Phys. Lett.*, 95, 103105 (2009).
[46] J. M. Bruneau, B. Bechevet, B. Valon, E. Butaud, *Optical Data Storage Topical Meeting 1997*, 104 (1997).
[47] S. K. Lin, I. C. Lin and D. P. Tsai, *Opt. Express*, 14, 4452 (2006).
[48] A. J. G. Mank, A. E. Ton Kuiper, H. A. G. Nulens, B. Feddes, and G. Wei, *Jpn. J. Appl. Phys.*, 46, 5813 (2007)
[49] J. H. Yoo, J. H. Lee, S. Y. Yim, S. H. Park, M. D. Ro, J. H. Kim, I. S. Park, and K. Cho, *Opt. Express*, 12, 4467 (2004).
[50] Y. C. Chang, J. Y. Chu, T. J. Wang, M. W. Lin, J. T. Yeh, and J.-K. Wang, *Opt. Express*, 16, 740 (2008).
[51] H. Raether, *Surface Plasmons on Smooth and Rough Surfaces and on Gratings* (Springer-Verlag, Berlin, 1988).
[52] *Handbook of optical constants of solids*, edited by E. D. Palik, (Academic, Press, New York, 1985).
[53] L. Yin, V. K. Vlasko-Vlasov, J. Pearson, J. M. Hiller, J. Hua, U. Welp, D. E. Brown, and C. W. Kimball, *Nano Lett.*, 5, 1399 (2005).
[54] A. Degiron and T. W. Ebbesen, *J. Opt. A: Pure Appl. Opt.*, 7, S90 (2005).

[55] E. Devaux, T. W. Ebbesen, J.-C. Weeber and A. Dereux, *Appl. Phys. Lett.*, 83, 4936 (2003).
[56] T. J. Wang, J. Y. Chu, Y. C. Chang, M. W. Lin, J. T. Yeh, and J. K. Wang, unpublished.

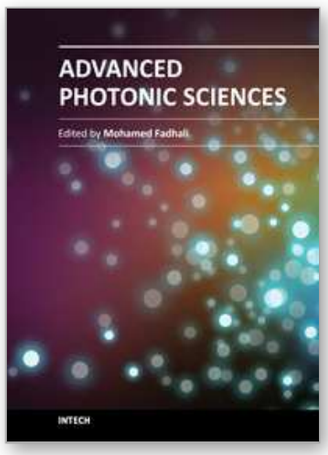

Advanced Photonic Sciences

Edited by Dr. Mohamed Fadhali

ISBN 978-953-51-0153-6
Hard cover, 374 pages
Publisher InTech
Published online 21, March, 2012
Published in print edition March, 2012

The new emerging field of photonics has significantly attracted the interest of many societies, professionals and researchers around the world. The great importance of this field is due to its applicability and possible utilization in almost all scientific and industrial areas. This book presents some advanced research topics in photonics. It consists of 16 chapters organized into three sections: Integrated Photonics, Photonic Materials and Photonic Applications. It can be said that this book is a good contribution for paving the way for further innovations in photonic technology. The chapters have been written and reviewed by well-experienced researchers in their fields. In their contributions they demonstrated the most profound knowledge and expertise for interested individuals in this expanding field. The book will be a good reference for experienced professionals, academics and researchers as well as young researchers only starting their carrier in this field.

InTech Europe
University Campus STeP Ri
Slavka Krautzeka 83/A
51000 Rijeka, Croatia
Phone: +385 (51) 770 447
Fax: +385 (51) 686 166
www.intechopen.com

InTech China
Unit 405, Office Block, Hotel Equatorial Shanghai
No.65, Yan An Road (West), Shanghai, 200040, China
中国上海市延安西路65号上海国际贵都大饭店办公楼405单元
Phone: +86-21-62489820
Fax: +86-21-62489821

IntechOpen